Simulation of VSPT Experimental Cascade Under High and Low Free-Stream Turbulence Conditions

Ali A. Ameri
The Ohio State University, Columbus, Ohio

Paul W. Giel
Vantage Partners, LLC, Cleveland, Ohio

Ashlie B. Flegel
Glenn Research Center, Cleveland, Ohio

NASA STI Program . . . in Profile

Since its founding, NASA has been dedicated to the advancement of aeronautics and space science. The NASA Scientific and Technical Information (STI) program plays a key part in helping NASA maintain this important role.

The NASA STI Program operates under the auspices of the Agency Chief Information Officer. It collects, organizes, provides for archiving, and disseminates NASA's STI. The NASA STI program provides access to the NASA Aeronautics and Space Database and its public interface, the NASA Technical Reports Server, thus providing one of the largest collections of aeronautical and space science STI in the world. Results are published in both non-NASA channels and by NASA in the NASA STI Report Series, which includes the following report types:

- TECHNICAL PUBLICATION. Reports of completed research or a major significant phase of research that present the results of NASA programs and include extensive data or theoretical analysis. Includes compilations of significant scientific and technical data and information deemed to be of continuing reference value. NASA counterpart of peer-reviewed formal professional papers but has less stringent limitations on manuscript length and extent of graphic presentations.

- TECHNICAL MEMORANDUM. Scientific and technical findings that are preliminary or of specialized interest, e.g., quick release reports, working papers, and bibliographies that contain minimal annotation. Does not contain extensive analysis.

- CONTRACTOR REPORT. Scientific and technical findings by NASA-sponsored contractors and grantees.

- CONFERENCE PUBLICATION. Collected papers from scientific and technical conferences, symposia, seminars, or other meetings sponsored or cosponsored by NASA.

- SPECIAL PUBLICATION. Scientific, technical, or historical information from NASA programs, projects, and missions, often concerned with subjects having substantial public interest.

- TECHNICAL TRANSLATION. English-language translations of foreign scientific and technical material pertinent to NASA's mission.

Specialized services also include organizing and publishing research results, distributing specialized research announcements and feeds, providing information desk and personal search support, and enabling data exchange services.

For more information about the NASA STI program, see the following:

- Access the NASA STI program home page at *http://www.sti.nasa.gov*

- E-mail your question to *help@sti.nasa.gov*

- Phone the NASA STI Information Desk at 757-864-9658

- Write to:
  NASA STI Information Desk
  Mail Stop 148
  NASA Langley Research Center
  Hampton, VA 23681-2199

Simulation of VSPT Experimental Cascade Under High and Low Free-Stream Turbulence Conditions

Ali A. Ameri
The Ohio State University, Columbus, Ohio

Paul W. Giel
Vantage Partners, LLC, Cleveland, Ohio

Ashlie B. Flegel
Glenn Research Center, Cleveland, Ohio

National Aeronautics and
Space Administration

Glenn Research Center
Cleveland, Ohio 44135

January 2015

Acknowledgments

Level of Review: This material has been technically reviewed by technical management.

Simulation of VSPT Experimental Cascade Under High and Low Free-Stream Turbulence Conditions

Ali A. Ameri
The Ohio State University
Columbus, Ohio 43235

Paul W. Giel
Vantage Partners, LLC
Cleveland, Ohio 44142

Ashlie B. Flegel
National Aeronautics and Space Administration
Glenn Research Center
Cleveland, Ohio 44135

Abstract

Variable-Speed Power Turbines (VSPT) for rotorcraft applications operate at low Reynolds number and over a wide range in incidence associated with shaft speed change. A comprehensive linear cascade data set obtained includes the effects of Reynolds number, free-stream turbulence and incidence is available and this paper concerns itself with the presentation and numerical simulation of conditions resulting in a selected set of those data. As such, post-dictions of blade pressure loading, total-pressure loss and exit flow angles under conditions of high and low turbulence intensity for a single Reynolds number are presented. Analyses are performed with the three-equation turbulence models of Walters-Leylek and Walters and Cokljat. Transition, loading, total-pressure loss and exit angle variations are presented and comparisons are made with experimental data as available. It is concluded that at the low freestream turbulence conditions the Walters-Cokljat model is better suited to predictions while for high freestream conditions the two models generate similar predications that are generally satisfactory.

Nomenclature

C_f magnitude of friction coeff. $|\tau_w|/0.5\rho_1 u^2_1$

Cp_s static pressure coef. $(P - P_{s2})/(P_{t1} - P_2)$

Cp_t total pressure coef. $(P_{t1} - P_t)/(P_{t1} - P_2)$

C_x axial chord

H blade span

HiTu   high free stream turbulence condition

i incidence angle

LoTu   low free stream turbulence condition

M_{is} Mach number based on isentropic expansion of inlet to exit static pressure

k turbulent kinetic energy

P pressure

Re Reynolds number based on Cx and isentropic exit conditions

S pitch

Tu turbulence intensity, $\sqrt{\overline{u'}_s^2}/U$

u'	fluctuating component of velocity
U	incoming free stream velocity
WL	Walters-Leylek Model
WC	Walters-Cokljat Model
x	axial coordinate
y	pitchwise coordinate
$y+$	dimensionless wall spacing
z	spanwise coordinate
ρ	density
τ	shear stress

Subscripts:

1	inlet condition
2	exit condition
s	streamwise
W	wall condition

Introduction

Accurate prediction of aerodynamic losses in blade rows operated under the conditions of low Reynolds number and at incidence challenges steady RANS methods. The state of the boundary layer (laminar, transitional, or turbulent) has a substantial effect on such losses and thus a realistic prediction of the flow depends on accurate modeling of transition. A discussion of various effects on losses as a function of Reynolds number is given in Reference 1. In a rather wide range of Reynolds numbers, one could find a combination of laminar, turbulent, transitional regimes with separated and attached boundary layers on the blade of a turbine. As for Variable-Speed Power Turbines, large incidence angles generated at lower shaft rotation rates give rise to higher lift but also the possibility of separation on the suction side while negative incidences due to higher rotation rates elevate the possibility of cove separation. These effects have consequences that need to be properly modeled for a reasonable accounting of the aerodynamic losses and exit angles. Suitable computational tools are needed in order to accurately model and assess the penalties associated with the change of variables resulting from a wide shaft-speed change. Blade row interaction and resulting unsteadiness has an important role to play (Ref. 2) in this complex interaction but is not within the scope of this work.

Previously, the capability of a published three-equation turbulence model, Walters and Leylek (WL) three-equation model (Ref. 3), to accurately predict the transition location for three-dimensional heat transfer problems was assessed at elevated turbulence levels (Ref. 4). Later, the performance of such advanced three-equation modeling was assessed for the Rolls-Royce VSPT blade (Ref. 5) but only the low turbulence intensity data were used as available. While the transition predictions were reasonable for the heat transfer problems, they were found to occur too far upstream for the VSPT case at low free stream turbulence.

Turbulence levels prevalent in engines are high. For the present work, both the low (0.3 percent) and high (12 percent) turbulence levels were considered and both the Walters-Leylek and a later version, Walters-Cokljat (WC) model (Ref. 6), were used. Results obtained with the later model of Walters and Cokljat, as will be shown in the present work, improve the predictions done in Reference 4.

One important reason for the choice of the turbulence models is the prevalence of "non-standard" grid topologies for which in complex three-dimensional flow computations of near-wall integral quantities are difficult to perform. In contrast to empirically based models, transport equations for transition and turbulence in References 3 and 6 use phenomenological models and do not require computation of any

boundary layer or integral quantities. In both the WL and WC models a modified form of the k-ω model supplemented with a transport equation for the "laminar kinetic energy" forms a three-equation model. The two models used are similar in the way they model transition via transfer (or redistribution) of energy from laminar kinetic energy to turbulence or pre-transitional instabilities. The newer model of Walters-Cokljat (Ref. 6) includes the effect referred to as "shear-sheltering," which is purported to remedy an issue with the earlier version and give a more accurate accounting of the effect of freestream turbulence length scale on the transition process. The formulation in Reference 6 contains typos that were subsequently fixed for example in Reference 7. A detailed comparison of the formulation of the two models and a critical analysis of WC model may be found in Reference 8.

VSPT Blade Experiment

A brief description of the cascade and a summary of the conditions for the experimental measurements used for this numerical validation are provided here. Additional details on the experiment and results are given in Reference 11.

The NASA Transonic Turbine Blade Cascade Facility (CW-22) is shown in Figure 1. The cascade's large scale and continuous run capability at engine relevant Mach numbers and Reynolds numbers allow for detailed blade heat transfer and aerodynamic studies. The blade geometry used in this test was a scaled two-dimensional midspan section of the VSPT second stage rotor (Ref. 9) shown in Figure 2 and the blade description is given in Table 1. The cascade for this test was made up of nominally ten blade passages. The blades were attached to a disk that can be rotated to set inlet flow angles (from axial) in the range $-17° \leq \beta_1 \leq +78.8°$. During this test, 10 incidence angles were examined (Refs. 10 and 11). Detailed three-dimensional flow field data were acquired at incidence angles of $+5.8°$ ($\beta_1 = +40.0°$) and $-36.7°$ ($\beta_1 = -2.5°$), which represent the cruise and takeoff flight mission points, respectively. These two mission points were used in the CFD verification in the current study. The angle settings are given in Table 2. The flow conditions as listed in Table 3 are the nominal conditions under which the CFD tests were run. The lowest achievable tunnel Reynolds number condition was higher than those at cruise. Nearly laminar flow was obtained by running the tunnel without the turbulence grid. High tunnel free stream turbulence is obtained by utilizing an upstream blowing grid located roughly five axial chords upstream of the blade row (Ref. 11). Some of the high free stream turbulence conditions are also transitional. Shown in Figure 2, the inlet conditions were measured at Station 0, located at 0.415 percent axial-chords upstream of the cascade. The inlet turbulence intensity without a turbulence grid was documented to range from 0.25 to 0.40 percent. The newer measurements with blown grid upstream indicate, for the cruise condition, turbulence levels in excess of 19 percent at a discreet location of 1.5 axial chord upstream of the cascade and 12 percent at the upstream measurement plane (Station 0). Those measurements at the takeoff condition were 10.5 and 8.5 percent, respectively.

For the low and high free stream turbulence studies total-pressure and exit flow angle data were acquired using a five-hole pitch-yaw probe. The probes were also installed in the Station 2 survey plane located approximately 7.0 percent axial-chord downstream of the blade trailing edge. The survey probe traversed three blade passages and half the span of the blade. For the two inlet angles considered in this study, pitchwise/spanwise surveys were taken which consisted of 26 spanwise surveys with 62 pitchwise points. For the low turbulence case, three-hole probes were used to survey the boundary layers but not for the high free stream turbulence study. The overall estimated uncertainty in flow angle was $\pm 1.5°$ and the overall estimated uncertainty in total-pressure coefficient was ± 0.8 percent.

Table 3 provides the experimental conditions which were used in the simulations. The turbulence for the present experiments was measured at two stations of approximately 1.5 and 0.4 axial- chords upstream of the blade row. These data may be used to compute a turbulence length scale for use as an inlet boundary condition for the computations as will be described in the next section.

The main measurement blades 4, 5, and 6, shown in Figure 2, were instrumented with static pressure taps at four spanwise locations. Blade 5 was fully instrumented with 44 taps along 10, 15, 30, and 50 percent of span.

For this study, the measured blade static pressure loadings at four spanwise locations, total-pressure loss as well as exit angle surveys at Station 2, were used for comparison with our computational results. The two incidence angles corresponding to cruise ($i = +5.8°$) and takeoff ($i = -36.7°$) rotational speeds were simulated.

Computational Method

The computer code Glenn-HT (Ref. 12) was used in this work. Glenn-HT is a Fortran 90 code. It uses structured multi-block grids. It is designed to be a multi-physics code and is currently capable of solving solid conduction and compressible fluid flow. To arrive at a steady solution, a finite- volume form of the unsteady compressible Reynolds-Averaged Navier-Stokes (RANS) equations are integrated in pseudo-time using an explicit Runge-Kutta solver in a multigrid driver. For the present exercise, the convective fluxes were discretized with a second order upwind scheme described in Reference 13. The diffusive terms were discretized using a second-order central differencing. The convective terms of the turbulence model equations were modelled using a first-order upwind method.

Simulations were run on a fine grid of nearly 7 million points. Average spacing of the first grid cells from the wall in terms of dimensionless y+ was computed to be approximately a value of 0.2. Earlier computations (Ref. 3) have shown this grid density to be highly conservative. Views of the grid showing every other point are shown in Figure 3. The grid was generated with the GridPro (Propex Operating Company, LLC) software (Ref. 14). The software used an elliptic solver to smooth an initial, algebraically generated, multi-block grid.

For the VSPT blade, taking advantage of the symmetry of the passage for the three-dimensional grid, only half of the span was gridded. The grid was constructed using multiple blocks in three-dimensional. As is the practice with grid generation when using GridPro, an inviscid grid was generated first and subsequently viscous grid was generated by clustering. The grid was clustered near the no-slip (blade and the endwall) surfaces. The spacing was chosen such that the first grid line away from the no-slip surfaces was at a dimensionless wall distance (y^+) of near unity to enable resolution of the laminar sublayer. In reality, the average value of this spacing was 0.2.

Boundary Conditions

The measured boundary conditions enable appropriate and accurate specification of the numerical boundary conditions imposed on the computations. Briefly, the exit boundary condition was a constant pressure boundary condition and was set according to the pressure ratio shown in Table 3. At the inlet, the boundary layer thickness was used to estimate a friction velocity (Ref. 15). Using the law of the wall/wake, a velocity profile was obtained which was subsequently converted into a total-pressure profile. In the free stream, the measured turbulence intensity and the turbulence length scale were used to specify the inlet conditions for the turbulence kinetic energy and specific dissipation (k and ω). The laminar kinetic energy, a variable in the Walters-Leylek turbulence model, was set to a very small value. A stable and satisfactory profile was established by specifying the inlet conditions in the free stream and allowing turbulence quantities to be extrapolated upstream within the boundary layer.

The turbulence length scale, as specified in computations of turbulent flows, represents the size of energy- containing eddies and is often specified as a percentage of a relevant length scale such as the passage span or blade axial chord. Values between 1 to 10 percent are customarily used. In the present study, available data were used to compute the length scale as described.

Length Scale Computation

In order to ascertain the appropriate value for the length scale which establishes the decay rate, computations were made using a three-dimensional sliver grid similar to the grid in Figure 3 covering the blade but having the upstream boundary at −1.5 axial-chord upstream. By iteratively adjusting the upstream value of the turbulence length scale, the turbulence level at the second location at $−0.415C_x$ was matched. The length scale computed at the second location was used as a boundary condition for the three-dimensional computations. For the rest of the computations (including the takeoff incidence angle) for which the upstream boundary was placed at $−0.415C_x$, the measured turbulence intensities and a length scale was specified.

Sensitivity to Length Scale Specification

The length scale determines the rate of decay of turbulence; the larger the length scale, the lower the physical rate of decay of turbulence. For the low turbulence intensity condition, turbulence intensity of 0.3 percent and a length scale of 0.3 percent axial chord were calculated and specified (Table 3) at the inlet plane to the computational domain. For the high turbulence intensity conditions, at takeoff speed, the inlet condition was also obtained from the experimental decay rate (1.0 percent of axial chord). At cruise speed however, the computed length scale value was problematic. In fact, an upper limit for the length scale was encountered beyond which the wake losses were found to vary rapidly and grow in a non-physical manner. Increasing length scale beyond this value was not accompanied by a further movement of the transition location upstream. The length scale computed from the data for this case was in this unphysical range. The length scale chosen was this upper value, 1.0 percent of axial chord, which was a quarter of the value which would have resulted from matching the decay of turbulence.

Results

Overview

The cases listed in Table 3 have been computed and the results are presented in this paper. The cases are for a single Reynolds number and two incidence angles corresponding to cruise and takeoff conditions at two free stream turbulence conditions; one at a very low and one at high free stream turbulence intensity. The cases are analyzed with Reynolds-Averaged Navier-Stokes analysis with transition and turbulence closure provided by WL and WC three-equation turbulence models (Refs. 3 and 6). Results for conditions of cruise and takeoff (Table 2) for both of the turbulence intensities considered are discussed in this section. The transition locations, loadings and total-pressure loss and exit angle distributions are discussed and compared to experimental measurements where available. The magnitude of skin friction coefficient on the blade suction and pressure surfaces at midspan are utilized to illustrate the process of transition. No data is available for skin friction while pressure loading in terms of static pressure coefficient, C_{ps}, and total-pressure losses C_{pt} at 7 percent of axial chord downstream of the trailing edge are compared to the measured experimental data.

Midspan Results

Results at the midspan are discussed first.

High Turbulence Conditions (HiTu)

Cruise incidence angle.—At high inlet turbulence intensity, the WL and WC models produce similar transition behaviors on the blade surface. Shown in Figure 6(a) on the suction side as well as the pressure side the boundary layer experiences a rather long transition before the flow becomes turbulent as compared to Figure 4(a). The change in the behavior of WL model is notable if compared to Figure 4(a). The abrupt transition at LoTu condition has changed to long transition for HiTu condition. WC model, on the other hand, as seen from Figure 4(a), behaves consistently as may be expected. Figure 6(b) shows the comparison with the measured pressure coefficient where the two models compare well with the experimental data. As for the total-pressure loss downstream of the wake, the two models perform similarly.

Low Turbulence Conditions (LoTu)

Cruise incidence angle.—For the LoTu condition, WL model shows early transition on the suction side at an axial location of approximately 35 percent as shown in Figure 4(a) by the abrupt rise in skin friction. The pressure side also shows transition to turbulence at about the same axial location. The WC model produces laminar flow on the suction side leading to separation at an axial location of 70 percent. Because the absolute value of skin friction is plotted, the negative values are reflected about the abscissa. The computation suggests that the separation bubble reattaches at around 75 percent axial chord, and then again separates at 85 percent axial chord. The second separation bubble is predicted not to close. Upon the initial reattachment, the dimensionless skin friction did not rise to the turbulent value, as was the case with the WL model, led to a second separation on the suction side. The inflection on the experimental pressure distribution near an axial location of 80 percent evident from Figure 4(b) suggests the boundary layer is indeed separated. The agreement of WC model with the data is indicative of the correctness of the prediction provided by the model for this case. Figure 4(c) compares the measured total-pressure loss coefficient with the predictions from WL and WC models at midspan. The WC model has a slightly better agreement in width to the experimental data.

Takeoff incidence angle.—Similar to the cruise case, the takeoff case shows early transition with WL model but slightly farther downstream on the suction side. Simulation with WC model, as in the case of cruise, shows a laminar boundary layer ending in a separation bubble. Here the boundary layer is experiencing near zero skin friction from a location of 80 to 90 percent axial chord at which location the separation bubble begins. Computations show the bubble to thin out near the trailing edge at an axial chord of 95 percent but not close.

On the pressure side, WL model produces a very small separation bubble. Reattachment produces a turbulent boundary layer similar to the cruise case in the downstream part. WC model produces a large separation bubble and a lower skin friction downstream of the separation bubble compared to the WL model which suggests that the state of the boundary layer is probably transitional.

Comparing to the experimental data for the pressure distribution, agreement is achieved by both the WL and WC models on the pressure side, WC model's production of a separation bubble on the suction side leads to agreement with the experimental data up to 85 percent axial chord. There is a discrepancy beyond this point. This may suggest that the state of the closure of the bubble may be the issue and not its existence or its location. Comparison of the total-pressure loss coefficient distribution in the wake showing increased loss production with the WC model may also be due to state of the bubble closure.

Overall WC model results seem to match the LoTu data and physical expectations better than the WL model. In Reference 8 a discussion is provided where the WC model is criticized for its tendency to produce large separation bubbles and no subsequent transition and re-separation which appears to be the case here. Nonetheless, the agreement with the data for pressure distribution and wake loss is satisfactory.

Takeoff incidence angle.—Shown in Figure 7, for the two models, the transition patterns and the magnitude of skin friction coefficient on the suction side are matched up to the point of separation. The location of transition on the suction side for the WC model is 10 percent chord farther downstream as compared to the WL model. On the pressure side, the WC model produces a separation bubble. The

slightly better agreement with the data on the pressure side with the WL model might suggest that the flow transitions around the leading edge on the pressure side and does not produce a separation bubble. The two models produce similar skin friction results beyond 50 percent chord on the pressure side.

Agreement with the experimental data for pressure Figure 6(b) is quite satisfactory. Total-pressure loss predictions in the wake at the midspan (Fig. 6(c)) appear to be of the proper height and width. The relatively good agreement between the two models comports with the relative similarity of the state of the boundary layer near the trailing edge resulting from the two models.

Three-Dimensional Variations

Overview

The experiments, as described earlier, were conducted using a linear cascade. There is significant three-dimensionality generated as a result of the thick inlet endwall boundary layer on the one hand and the near endwall cross passage flow on the other hand. The latter is amplified due to increased incidence at the cruise condition which results in higher loading. In our experiment, for the high free stream turbulence conditions, boundary layer thickness is substantially reduced by the turbulence grid although there still exist sizeable boundary layer at the inlet (Table 3). This caused a reduction in three-dimensionality of the flow field for the HiTu cases compared to the LoTu cases.

In this section, the computed skin friction on all the walls, the spanwise loading on the blades at specific spanwise locations, as well as the distributions of the total pressure loss coefficient and exit angle at a location of 7 percent downstream of the blade cascade (Station 2) will be presented.

Skin Friction Coefficient

Skin friction coefficient was computed over both the suction and pressure side surfaces and the endwall. Figures 8 to 11 show the computed skin friction coefficient for the LoTu and HiTu cases at the cruise and takeoff conditions. Each figure contains two paired sets of computations with the WC and WL models. The pair of figures show contour plots on the suction side and pressure side surfaces. It was stated before that the high turbulence condition was accompanied by a smaller inlet boundary layer thickness thus leading to reduced three-dimensionality. In addition, blades at the takeoff condition were not as highly-loaded compared to the cruise condition which also led to reduced three-dimensionality. This is seen to apply to the C_f distribution on the surfaces. Cases with high turbulence intensity and/or takeoff condition which are lightly loaded demonstrate less variation in spanwise direction. The shape of transition process generally follows those shown earlier in line plots. For the LoTu cruise condition shown in Figure 8, WC model produces a three-dimensional transition which seems to have been triggered along the pressure side leg of horseshoe vortex running up on the suction side. WC and WL models differ in their predictions more significantly for the LoTu cases as shown with the line plots (Figs. 4 to 7) are similar for the HiTu cases on the suction side and differ on the pressure sides.

For the HiTu cases the values of the endwall friction factor are similar for the two models. For the LoTu cases the results differ. Based on the improved agreement on the blade surface when using WC model, the endwall cases for that model garner more confidence.

Pressure Loading

Figures 12 and 13 show, respectively show spanwise blade loading at low and high freestream turbulence conditions. WL model results are shown on the left side column and WC results are on the right. The top row shows the loadings for the cruise condition and the bottom row pertains to the takeoff condition. Plots are shown for four spanwise locations of 10, 15, 30, and 50 percent of span. Experimental results were measured on three blades but the legend is consolidated in this paper. Further details are available in the accompanying paper detailing the relevant experiments.

For the LoTu conditions at cruise, the better agreement on the suction side for the WC model at midspan was already discussed. Other spanwise locations agree well with the experimental data and neither model enjoys an advantage. For the takeoff condition at LoTu the WC model shows better agreement up to 85 percent axial chord after which the agreement deteriorates perhaps due to laminar bubble closure discussed earlier. The open separation bubble is prevalent down to near the endwall.

Figure 9 shows the loading at HiTu condition. Under high free stream turbulence conditions separation is not an issue and the endwall boundary layer thickness and three-dimensionality is reduced. The agreement with the data for both the cruise and takeoff conditions appears to be good at all spanwise data points.

Wake Losses

Low Tu.—CasesComputed total-pressure losses at midspan and comparisons with the experimental data were presented using the two chosen turbulence models in Figures 4 to 7. Three-dimensional variations were measured across the passage at an axial location of 7 percent axial chord downstream of the trailing edge. Figures 14 to 17 show the measured total-pressure loss profile (Ref. 10) and the predicted values with WL model and WC models. The results are plotted (repeated) over two pitches and across half the span. The measurements included the endwall boundary layer for the LoTu cases but not for the HiTu cases. All the figures show elevated losses in the wakes and near the endwall as well as low total-pressure losses in between the blades as expected.

Figure 14(a) shows that there are two "islands" of high total-pressure loss along the wake-line near the midspan in the experimental measurements. The lower one is due to the pressure side leg of the horseshoe vortex and that can be verified by inspecting the computational results. The one near the midspan is due to the separation bubble. This may be deduced by comparing the map obtained using the WL model which does not produce a separation bubble and the WC model which does produce a bubble and the fact that WC model agrees better with the experimental measurements. Overall, WC model is in better agreement with the experimental data. In Figure 11, takeoff results are shown where the passage vortex is weakened relative to the cruise conditions, as expected, and loss cores are placed near the endwall instead of moving up the blade. Three-dimensionality is greatly reduced compared to the cruise results. Both the WL model and WC model produce good results but near the endwall WC model shows better agreement with the experimental data.

High Tu cases.—For the high free stream turbulence cases at cruise condition, the WL and WC model show a larger wake than the data although the WC model performs slightly better. The loss core due to the pressure side leg of horseshoe vortex appears to be over predicted. For the takeoff condition, again, the loss core is small and the agreement of both models with the data is quite reasonable. Note that the near endwall measurements were not taken for the HiTu cases. Also, note the slight variation of the experimental contour map between the wakes.

Flow angles.—Prediction of exit angle is important as it is a determining factor in the calculation of the power generated by the turbine rotor. For the cascade considered here the exit metal angle is –55.54° and as such the contours legends are setup to center around this value. Figures 18 to 21 show the measured exit angles across a plane at Station 2, namely, 7 percent axial chord downstream of the trailing edge. The plots show how highly three-dimensional the flow is. In general it may be observed that the predictions agree rather closely with the experimental data when the takeoff conditions are examined. For the cruise conditions, the agreement seems to be within one or 2°. There are local regions for which this estimate may not be accurate. Along the wake region the experimental data for the cruise condition signal large deviations from the metal angle. These regions may be inside separation bubbles and as such are subject to larger experimental error.

Summary and Conclusions

For the VSPT, flow transition/separation has been identified as an important process. Large variations in incidence angles and low Reynolds numbers require models that can reasonably compute these flows. Numerical modeling of the three-dimensional flow in a two-dimensional transonic linear cascade was performed at the two incidence angle conditions corresponding to takeoff and cruise and for conditions of low and high free stream turbulence. Both the Walters-Leylek (WL) and Walters-Cokljat (WC) models were utilized. WL model was found to lead to early transition for the low turbulence conditions used in an earlier work (Ref. 5) and thus the WC model was also used for its reported improved transition capability at lower turbulence conditions.

As for transition modeling, the results of the present study show that at low free stream turbulence WC model provides improved predictions compared to WL model. WL model did not predict transition well at low turbulence conditions as they were too early. Transition predictions with the WC model leads to a more physical and consistent set of results at both the high and low freestream turbulence. At the high freestream turbulence level the two models performed similarly.

As for loading predictions, at low freestream turbulence, loading is better predicted by the WC model. One issue encountered with the WC model at low free stream turbulence was the production of a long separation bubble which did not close and led to a discrepancy with the experimental data near the trailing edge on the suction side. This agreed with the observations made by Turner (Ref. 8). This behavior was consistent in the spanwise direction and led to a small discrepancy with the experimental data. Elsewhere, for both the low and the high *Tu* conditions, the three-dimensional blade loadings agreed reasonably well with the experimental measurements.

Total-pressure losses downstream of the trailing edge were generally in good agreement with the data at least in shape and width of the wake. Two-dimensional maps at Station 2 showed good agreement at LoTu with the WC model and fair agreement with the WL model. At HiTu, both models over-predict the size of the loss core. A shift with respect to the experimental data was present in the midspan wake profile that indicated exit flow angle deviation.

Flow angle contours at Station 2 suggest that the predictions agree with the data to within 2° with the exception of wake regions near the trailing edge which could be caused due to experimental errors.

In view of the fact that WL model failed to predict transition at LoTu conditions while it performed well at HiTu conditions and WC model produced reasonable transition predictions at low and high free stream turbulence conditions we conclude that the WC model is preferable to WL model for VSPT computations.

Finally, it is highly desirable that the dissipation rate of turbulence, set by the length scale at the inlet boundary to the simulations, be based on experimental measurements. While the experiments provided enough information to compute the appropriate length scale, our attempts at specifying a decay rate based on experimental conditions for the high free stream turbulence computations did not lead to physically sensible results. As such, length scale was chosen based on the ability to produce physical results. The inlet turbulence was quite high and perhaps the decay rate was outside the calibration of the model. Unfortunately data with an intermediate turbulence level was not at hand and thus the issue remains to be further investigated.

References

1. Lou, Weiliang and Hourmouziadis, J., 2000, "Separation Bubbles Under Steady and Periodic-Unsteady Main Flow Condition," ASME Transaction, Journal of Turbomachinery, Vol. 122, No. 4.
2. Welch, G.E., 2010, "Assessment of Aerodynamic Challenges of a Variable-Speed Power Turbine for Large Civil Tilt-Rotor Application," Proc. AHS Int. 66th Annual Forum, May; also NASA/TM—2010-216758, Aug, 2010.

3. Walters, D.K. and Leylek, J.H., 2005, "Computational Fluid Dynamics Study of Wake-Induced Transition on a Compressor-Like Flat Plate," *ASME Journal of Turbomachinery*, Volume 127, Issue 1, 52 (12 pages).
4. Ameri, A., 2012 "Use of Transition Modeling to Enable the Computation of Losses for the Variable-Speed Power Turbine," GT2012-69591, Turbo Expo, Copenhagen, Denmark.
5. Ameri, A., Giel, Paul W., McVetta, Ashlie B., "Validation of a CFD Methodology for Variable Speed Power Turbine Relevant Conditions," GT2013-95030, ASME Turbo Expo., Technical Conference and Exposition, San Antonio, Texas, USA.
6. Walters, D. Keith and Cokljat, Davor, 2008, "A Three-Equation Eddy-Viscosity Model for Reynolds-Averaged Navier-Stokes Simulation of Transitional Flows," *ASME Journal of Turbomachinery,* Volume 130, 121401-01 to-121401-13.
7. Furst, Jiri, "Numerical Simulation of Transitional Flows with Laminar Kinetic Energy," Engineering Mechanics, Vol. 20, 2013, No. 5, p. 379-388.
8. Turner, Clare, 2012, Laminar Kinetic Energy Modelling for Improved Laminar-Turbulent Transition Prediction, PhD Thesis. Manchester, UK: The University of Manchester; 2012.
9. Ford, A., Bloxham, M., Turner, E., Clemens, E. and Gegg, S., 2012, "Design Optimization of Incidence-Tolerant Blading Relevant to Large Civil Tilt-Rotor Power Turbine Applications," NASA/CR—2012-217016, Dec.
10. McVetta, A.B., Giel, P.W, Welch, G.E., 2013, "Aerodynamic Measurements of a Variable-Speed Power-Turbine Blade Section in a Transonic Turbine Cascade at Low Inlet Turbulence," GT2013-94695, to be presented at 2013 ASME Turbo Expo.
11. Flegel, Ashlie B., Giel, Paul W., Welch, Gerard E., 2014, "Aerodynamic Effects of High Turbulence Intensity on a Variable-Speed Power-Turbine Blade with Large Incidence and Reynolds Number Variations," AIAA paper number 1946083, presented at the 50th AIAA/ASME/SAE/ASEE Joint Propulsion Conference, Cleveland, Ohio, July 2014.
12. Steinthorsson, E., Liou, M.S., and Povinelli, L.A., 1993, "Development of an Explicit Multiblock/Multigrid Flow Solver for Viscous Flows in Complex Geometries," AIAA-93-2380.
13. Hunyh, H.T., 1996, "Accurate Upwind Methods for Euler Equation," *SIAM J. Numer. Anal.*, Vol. 32, No. 5, pp. 1565-1619.
14. GridPro, Program Development Corporation, White Plains, N.Y.
15. White, Frank, M. 1991, *Viscous Fluid Flow*, Second Edition, McGraw-Hill Inc., New York.

TABLE 1.—BLADE DESCRIPTION

Geometry	Value
Axial chord, C_x	180.57 mm (7.109 in.)
True chord	194.44 mm (7.655 in.)
Pitch, S	130.00 mm (5.119 in.)
Span, H	152.40 mm (6.000 in.)
Throat diameter	72.85 mm (2.868 in.)
Leading edge diameter	15.16 mm (0.597 in.)
Trailing edge diameter	3.30 mm (0.130 in.)
Stagger angle	20.35°
Inlet metal angle	34.2°
Uncovered turning	19.47°
Exit metal angle	−55.54°

TABLE 2.—ANGLE SETTINGS

Inlet angle, β_1	Incidence angle, i
40.0° (Cruise)	+5.8°
−2.5° (Takeoff)	−36.7°

TABLE 3.—FLOW CONDITIONS USED IN THE SIMULATIONS

Inlet angle β_1	Exit Re_{Cx}	Press. ratio	Exit M_{IS}	δ_{inlet} or δ_1, in.	$Tu_{in}\%$ at −1.5 C_x	$Tu_{in}\%$ at −0.415 Cx
40.0°	536,000	1.412	0.72	1.44	0.4	0.3
−2.5°	532,000	1.348	0.67	1.50	0.4[a]	0.3[a]
40.0°	536,000	1.412	0.72	0.73	19.5	12.0
−2.5°	532,000	1.348	0.69	0.76	10.5	8.5

[a]Measured for the 40° incidence but deemed valid for this case.
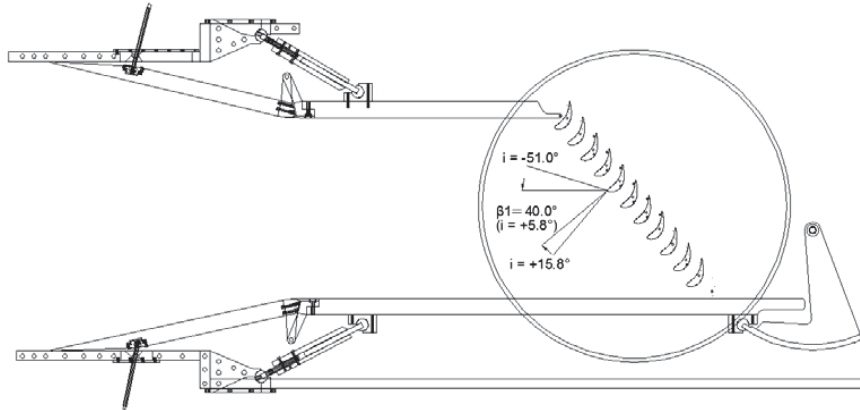
Figure 1.—Overall view of NASA Glenn's transonic cascade facility.
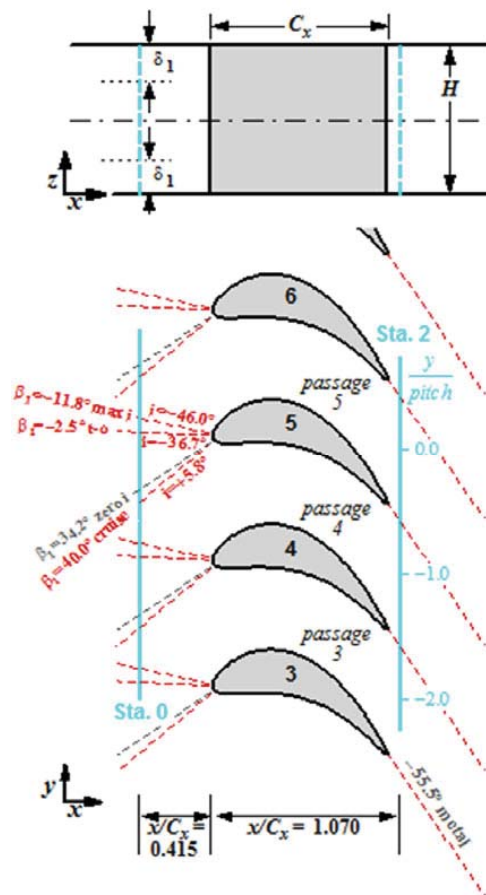
Figure 2.—Blade geometry and exit survey plane location.
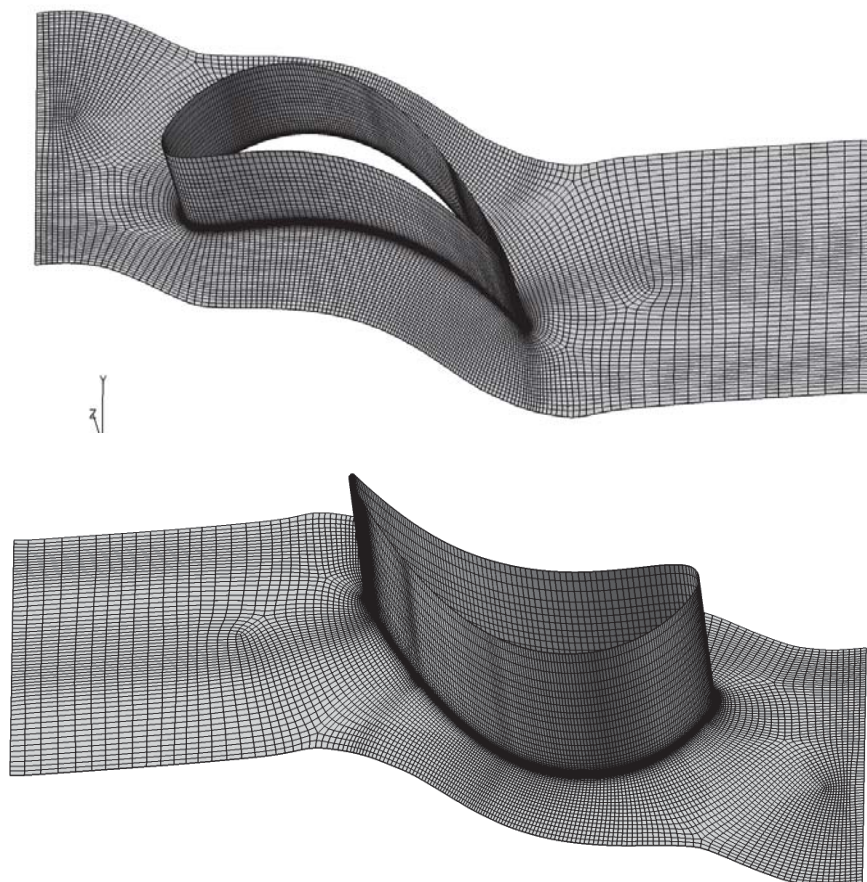
Figure 3.—Multi-block grid showing every alternate point on the endwall and blade surfaces.
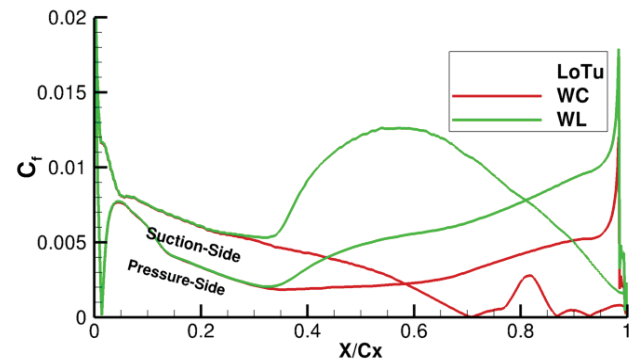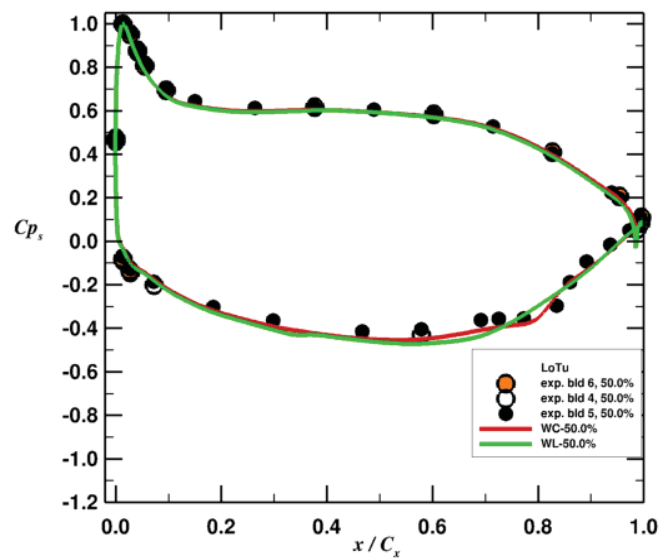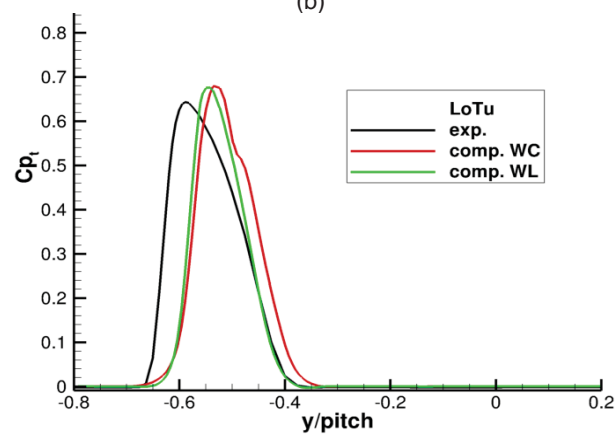
Figure 4.—Cruise at LoTu, (a) Skin friction, (b) Static pressure coefficient and (c) C_{pt} distribution in the wake at the midspan.
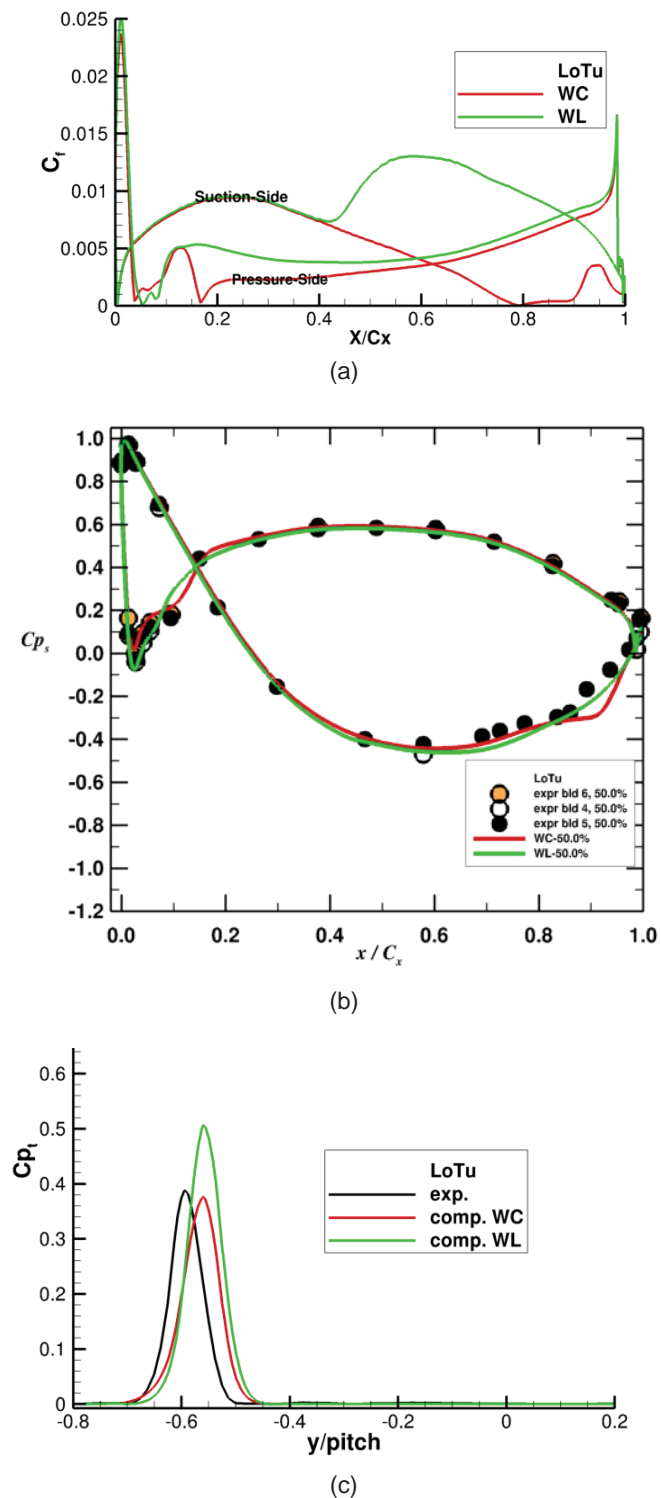
Figure 5.—Takeoff at LoTu, (a) Skin friction, (b) Static pressure coefficient and (c) C_{pt} distribution in the wake at the midspan.

(a)

(b)

(c)
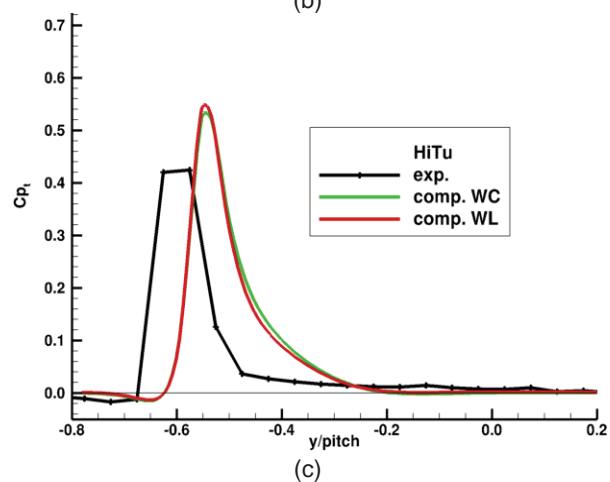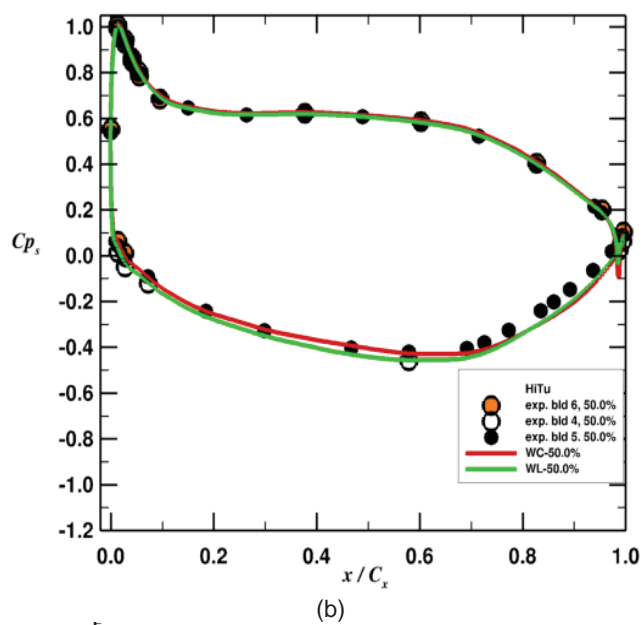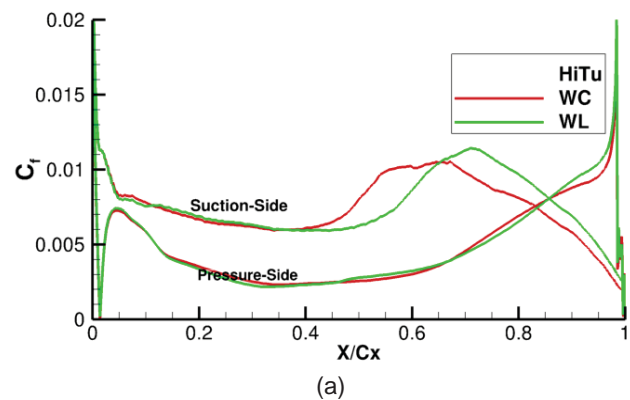
Figure 6.—Cruise at HiTu, (a) Skin friction, (b) Static
pressure coefficient and (c) C_{pt} distribution in the
wake at the midspan.

(a)

(b)

(c)
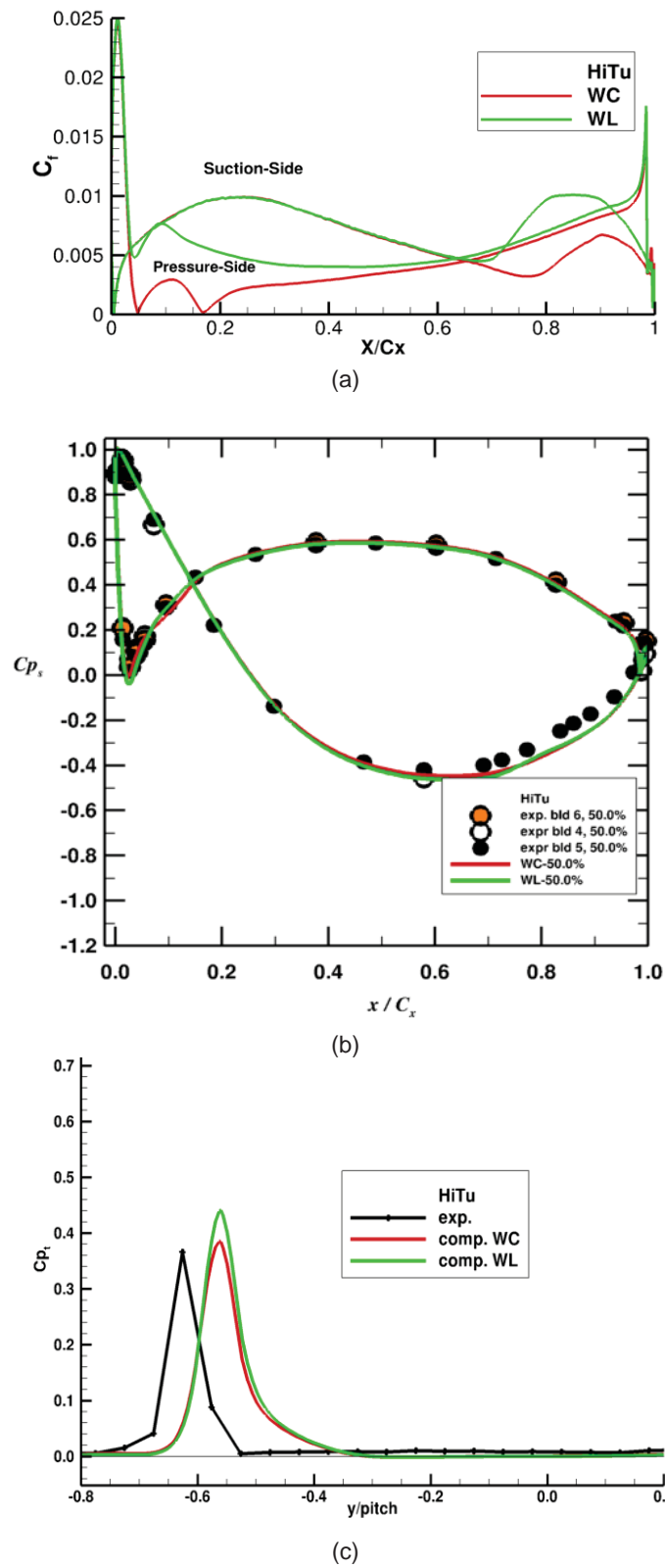
Figure 7.—Takeoff at HiTu, (a) Skin friction, (b) Static pressure coefficient and (c) C_{pt} distribution in the wake at the midspan.
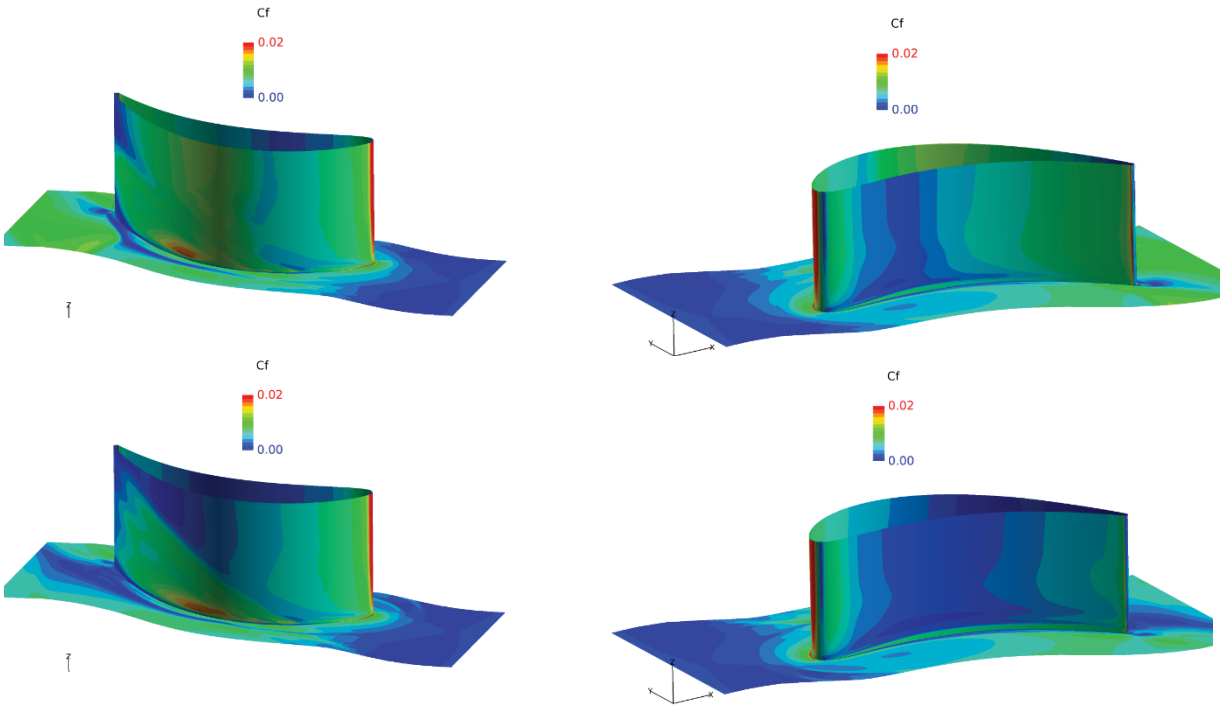
Figure 8.—Suction-side (left) and pressure-side (right) skin-friction coefficient contours on the blade surface computed using WL model (top) and WC model (bottom) row at the cruise and LoTu.
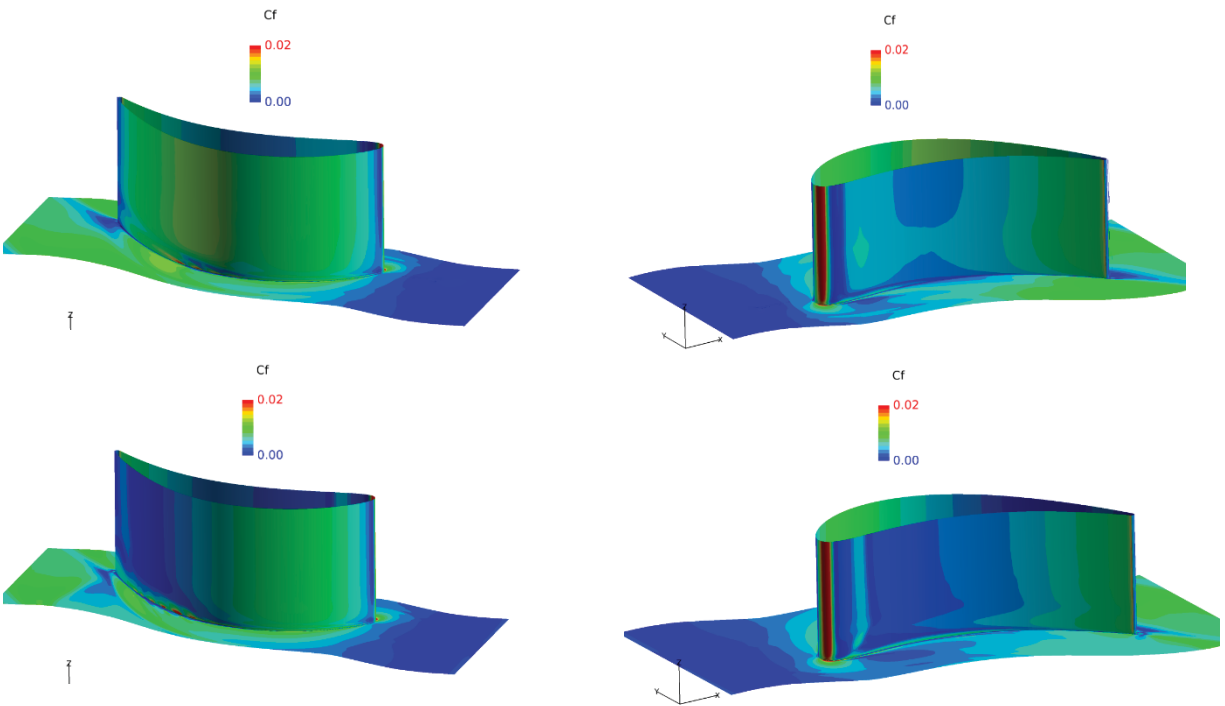
Figure 9.—Suction-side (left) and pressure-side (right) skin-friction coefficient contours on the blade surface computed using WL model (top) and WC model (bottom) row at the takeoff and LoTu.
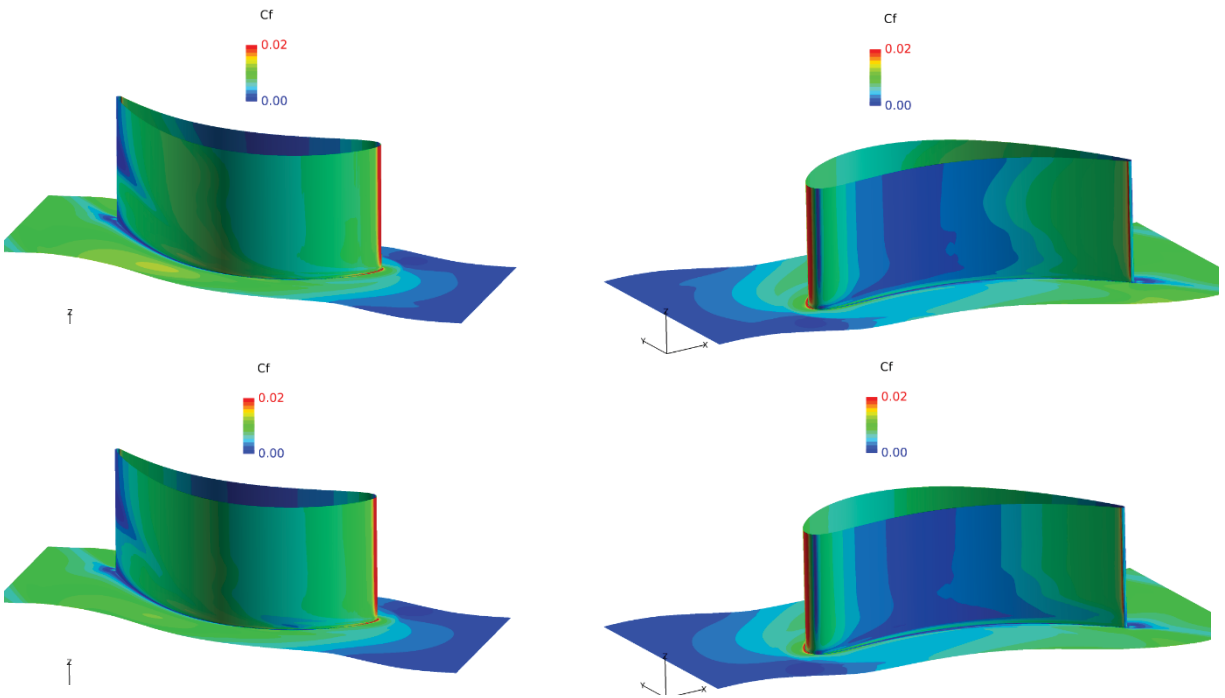
Figure 10.—Suction-side (left) and pressure-side (right) skin-friction coefficient contours on the blade surface computed using WL model (top) and WC model (bottom) row at the cruise and HiTu.
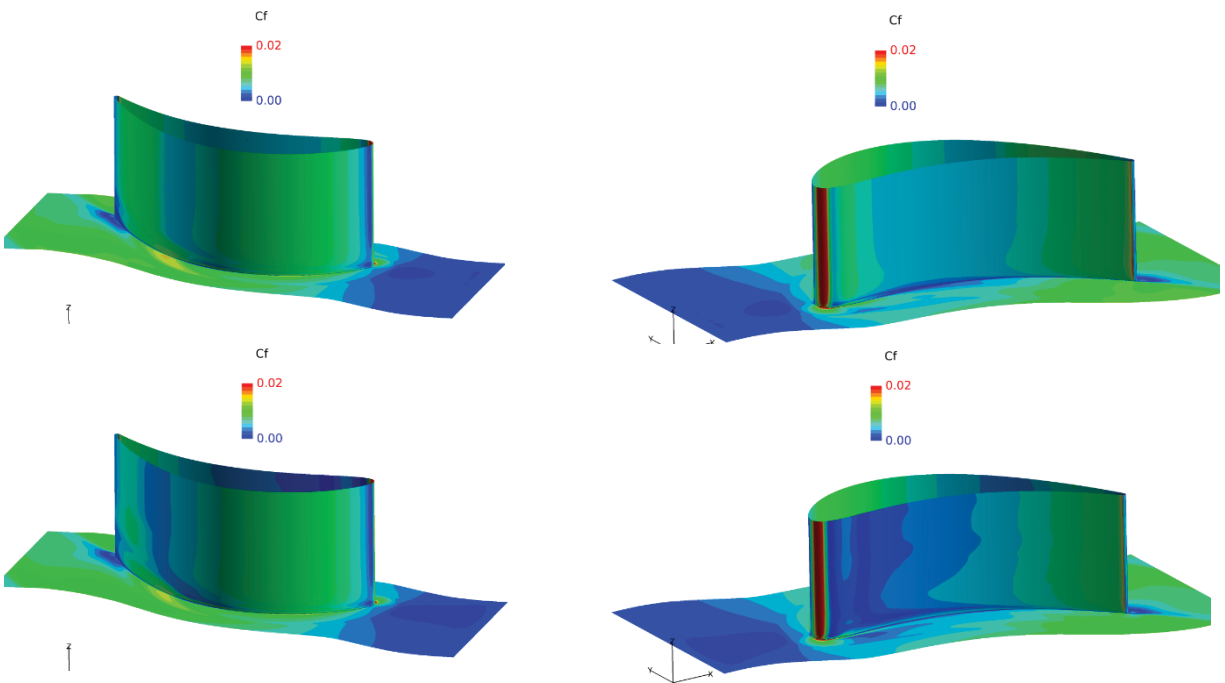
Figure 11.—Suction-side (left) and pressure-side (right) skin-friction coefficient contours on the blade surface computed using WL model (top) and WC model (bottom) row at the takeoff and HiTu.
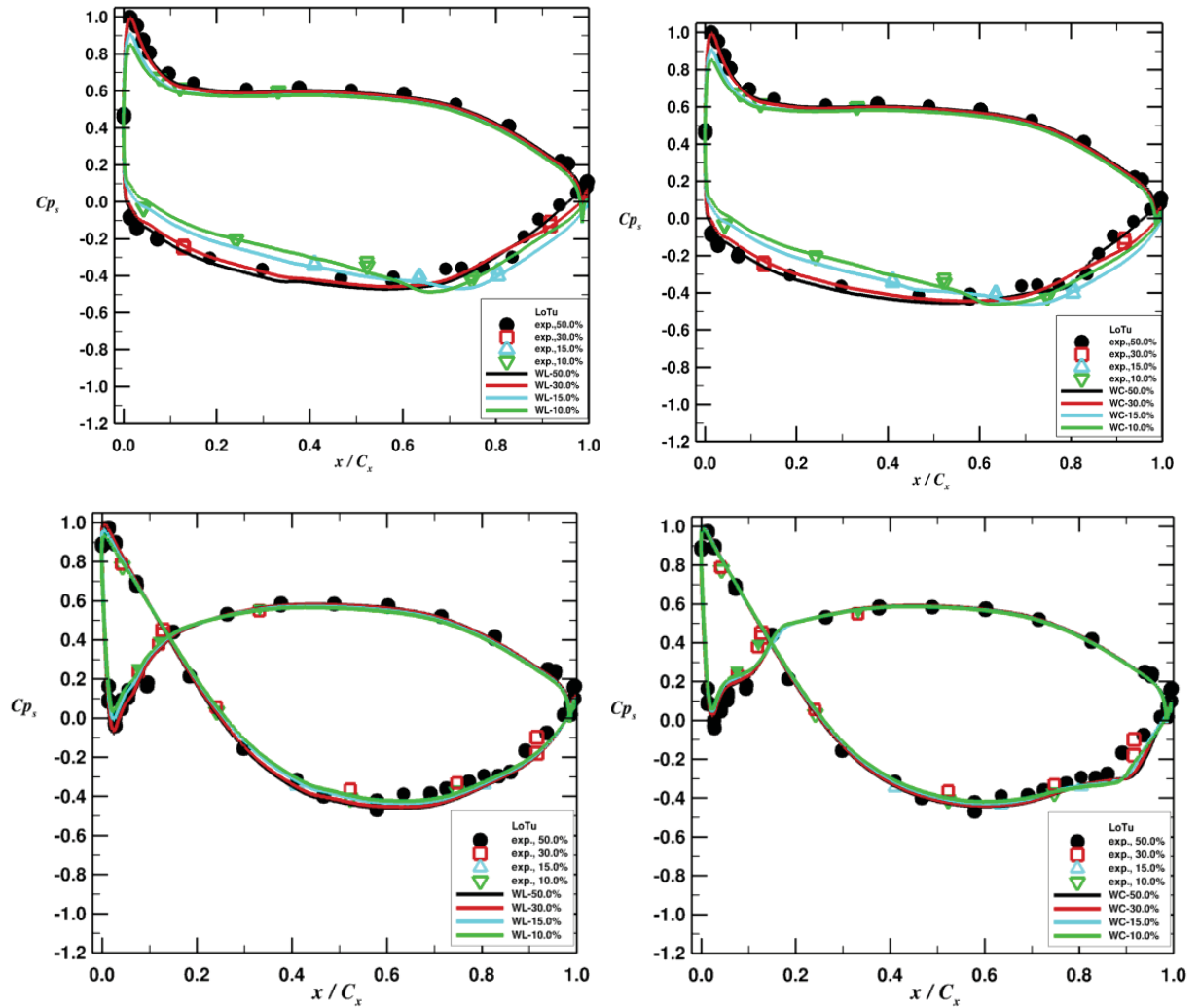
Figure 12.—Spanwise blade loading at LoTu. WL model results are shown on the left column and WC model are on the right column. Upper row is for the cruise condition and lower row is for the takeoff condition.
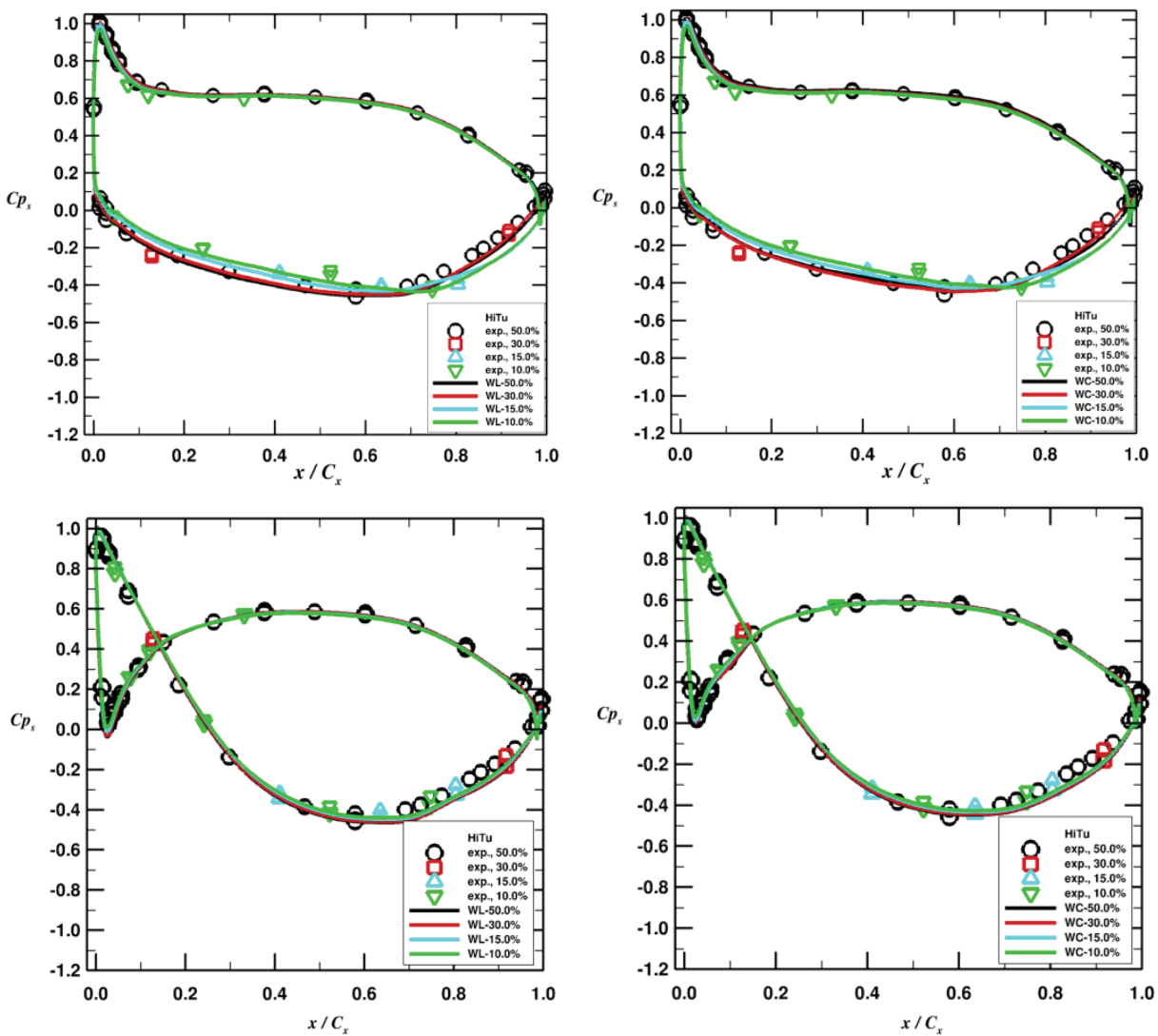
Figure 13.—Spanwise blade loading at HiTu. WL model results are shown on the left column and WC model are on the right column. Upper row is for the cruise condition and lower row is for the takeoff condition.
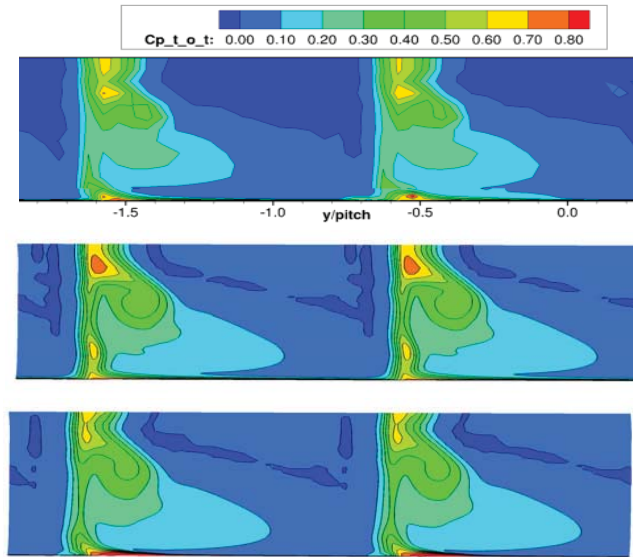
Figure 14.—Total-pressure loss C_{pt} at Station 2 with LoTu,
cruise condition, (a) Exp., (b) WL model and (c) WC model.
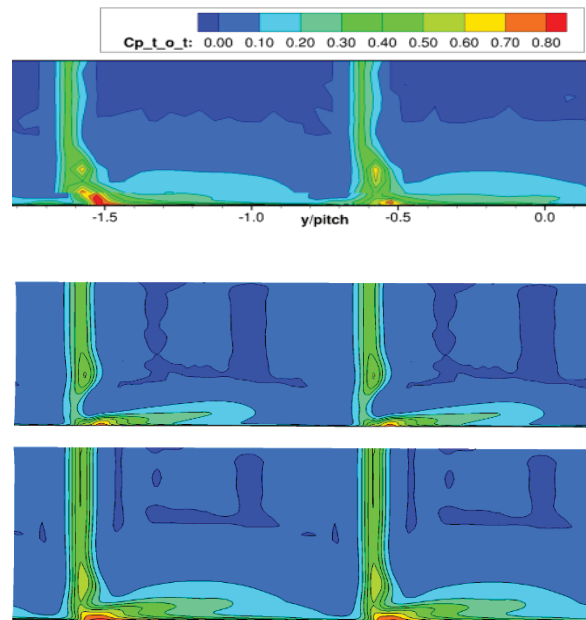
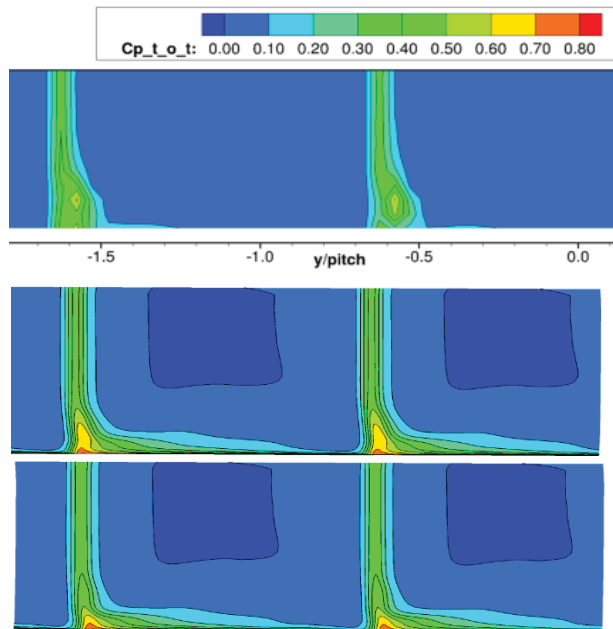Figure 15.—Total-pressure loss C_{pt} at Station 2 with
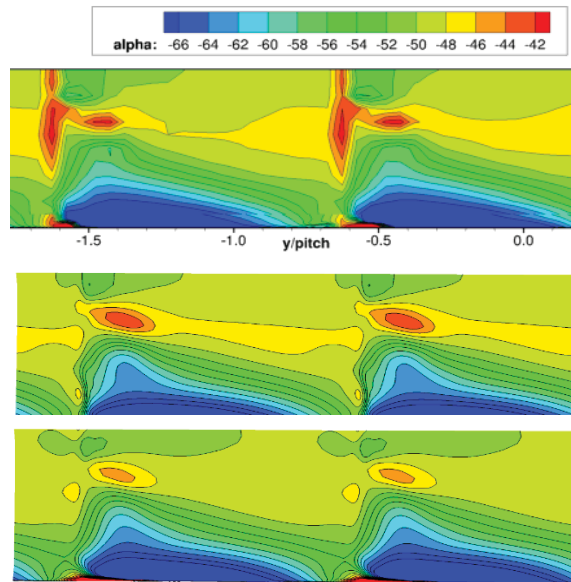LoTu, takeoff condition, (a) Exp., (b) WL model and
(c) WC model.
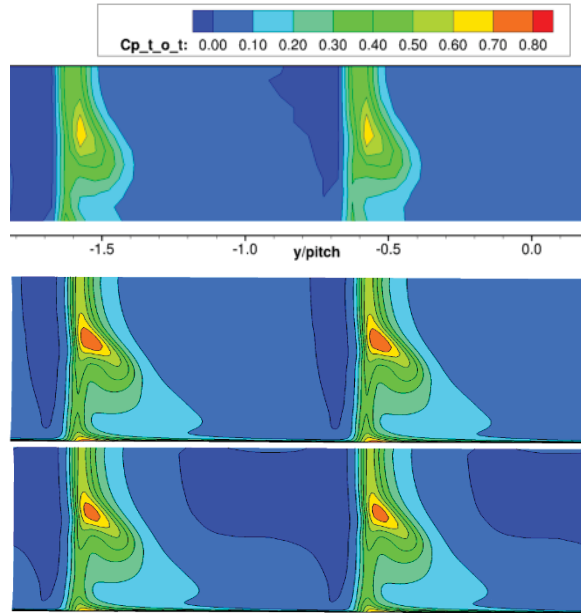
Figure 16.—Total-pressure loss C_{pt} at Station 2 with HiTu, cruise condition, (a) Exp., (b) WL model and (c) WC model.

Figure 17.—Total-pressure loss C_{pt} at Station 2 with HiTu, takeoff condition, (a) Exp., (b) WL model and (c) WC model.

Figure 18.—Exit angle at Station 2 with LoTu, cruise condition, (a) Exp., (b) WL model and (c) WC model.
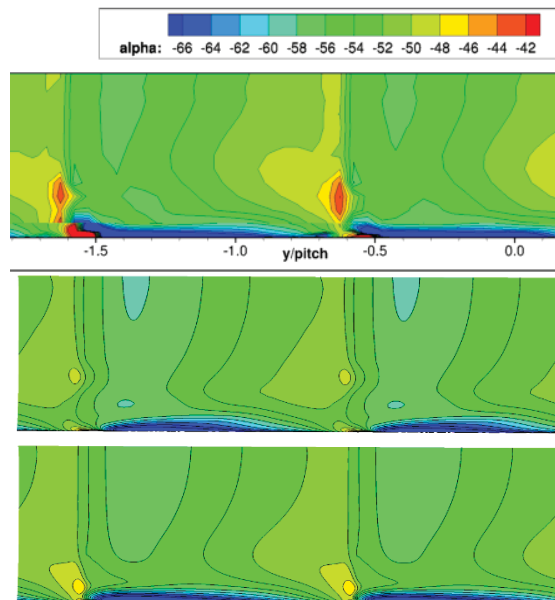

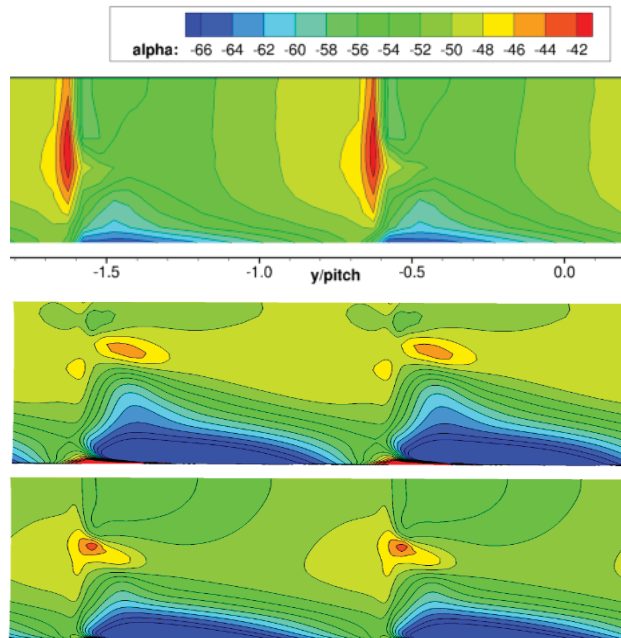Figure 19.—Exit angle at Station 2 with LoTu, takeoff condition, (a) Exp., (b) WL model and (c) WC model.

Figure 20.—Exit angle at Station 2 with HiTu, cruise
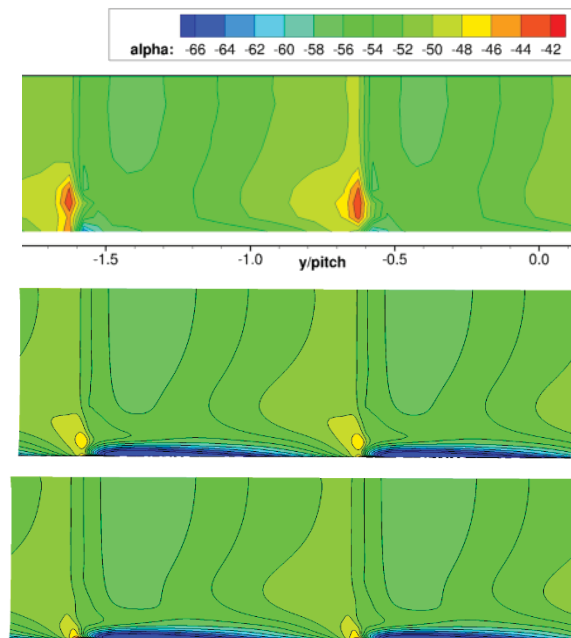condition, (a) Exp., (b) WL model and (c) WC model.

Figure 21.—Exit angle at Station 2 with HiTu,
takeoff condition, (a) Exp., (b) WL model and
(c) WC model.